RSC Advances

PAPER

View Article Online
View Journal | View Issue

Cite this: *RSC Adv.*, 2025, **15**, 7876

Complete inhibition of localized corrosion in 5Cr steel under a water-saturated supercritical CO_2 environment through Al microalloying

Fubing Liu, Hangqi Li, Yunan Zhang, Rongdie Zhu and Jinyang Zhu *

Received 25th January 2025
Accepted 6th March 2025

DOI: 10.1039/d5ra00591d

rsc.li/rsc-advances

To address the critical corrosion challenges faced by metal pipelines in carbon capture, utilization, and storage (CCUS) technologies, the study prepared a series of novel Fe-5Cr-(0–3)Al alloy steels. The corrosion resistance of these alloys in a water-saturated supercritical CO_2 (sc-CO_2) environment was systematically investigated. The results revealed that increasing Al content significantly reduced the corrosion rate. When the Al content reached 2 wt%, the average corrosion rate decreased by 68% of that of conventional 5Cr steel, and localized corrosion was completely suppressed. Furthermore, the study explores the underlying mechanisms of localized corrosion, shedding light on the key factors contributing to this remarkable performance. These findings not only demonstrate the alloys' potential as a cost-effective, high-performance solution for CCUS applications but also provide a scientific foundation and technical guidance for the development of future corrosion-resistant steels.

1 Introduction

Global climate change has become a critical global issue, with reducing CO_2 emissions increasingly recognized as essential for mitigating climate-related challenges.[1,2] Studies have established CO_2 emissions as the primary driver of global warming. In light of rapid advancements in energy systems and carbon capture, utilization, and storage (CCUS) technologies, the corrosion resistance of materials used in these systems is crucial for ensuring operational safety, efficiency, and cost-effectiveness.[3–6]

In CCUS applications, CO_2 is typically compressed to a supercritical state (supercritical CO_2, with a critical temperature of 31.1 °C and pressure of 7.38 MPa). Due to its elevated temperature, high pressure, and coexistence with H_2O, supercritical CO_2 (sc-CO_2) presents significant challenges to the corrosion resistance of metallic materials (for example, carbon steel, low-chromium alloy steel).[7–9] While dry CO_2 is non-corrosive, the presence of free water or water content below CO_2 solubility can lead to condensation on carbon steel surfaces during transport or injection, triggered by pressure and temperature fluctuations. This condensation promotes localized corrosion.[10,11] In subsea CO_2 sequestration, the extraction effect of sc-CO_2, coupled with water evaporation, results in saturated water in the upper layer of the sc-CO_2 phase, posing a severe threat of localized corrosion to pipeline inner walls. Here, the localized corrosion rate often surpasses the average corrosion rate, with pitting depths reaching up to 20 μm.[12,13] Although research has shown that increased water content exacerbates corrosion in sc-CO_2 environments, the mechanisms of localized corrosion remain poorly understood.[14–17]

To address corrosion in sc-CO_2 environments, utilizing corrosion-resistant stainless steel is an effective protective measure. However, its high initial cost limits widespread application.[18–20] In contrast, low-chromium (low-Cr) steel, offering a balance of good corrosion resistance and cost-effectiveness, has emerged as a research hotspot for CO_2 pipeline transport. Alloying low-Cr steel to enhance its resistance to CO_2 corrosion is now a primary focus, aiming to develop cost-effective, high-performance alloy steels.[21–23] Aluminum (Al), with its high chemical reactivity, forms a dense protective layer during the early stages of corrosion, improving the material's resistance to localized corrosion. Studies have shown that 3Cr steel with added Al significantly reduces localized corrosion susceptibility in CO_2/O_2 environments.[24,25]

Based on these insights, this study developed a series of novel low-Cr alloy steels by modifying conventional 5Cr steel with varying Al contents (1–3 wt%). The localized corrosion behavior of these alloys in water–saturated sc-CO_2 phase was systematically investigated. By exploring the corrosion mechanisms, this research provides critical theoretical support and technical guidance for optimizing low-Cr alloy steel composition, enhancing corrosion resistance, and extending the service life of equipment.

2 Experimental

2.1 Materials

Three novel Al-containing low-Cr steels (5Cr1Al, 5Cr2Al, and 5Cr3Al) were prepared based on conventional 5Cr steel by

National Center for Materials Service Safety, University of Science and Technology Beijing, Beijing 100083, China. E-mail: zhujinyang@ustb.edu.cn

Table 1 Chemical composition of tested steels (wt%)

Steel	C	Si	Mn	Cr	Al	Mo	Nb	S, P	Fe
5Cr	0.07	0.20	0.55	5.00	0.00	0.15	0.05	0.008	Balance
5Cr1Al	0.07	0.20	0.55	5.00	1.00	0.15	0.05	0.008	Balance
5Cr2Al	0.07	0.20	0.55	5.00	2.00	0.15	0.05	0.008	Balance
5Cr3Al	0.07	0.20	0.55	5.00	3.00	0.15	0.05	0.008	Balance

introducing varying aluminum contents (1–3 wt%), with their chemical compositions detailed in Table 1. Conventional 5Cr steel was used as the control. All materials were prepared through a combination of melting, rolling, and heat treatment processes.

The rolling procedure was conducted as follows: steel ingots were heated at 1200 °C for 1 hour, followed by removal of the oxide layer and subsequent rolling. The hot-rolling process involved two passes of rough rolling, with an initial temperature of 1150 °C, a final temperature of ≥1000 °C, and a reduction rate exceeding 50%. This was followed by three passes of finish rolling, with an initial temperature between 900–920 °C and a final temperature of 780–820 °C. The final steel plates had a thickness of approximately 5 mm, with a cooling rate of 15–20 °C s^{-1}. Heat treatment consisted of quenching at 900 °C (water cooling) and tempering at 660 °C (air cooling). The microstructure of the 5Cr steel consisted of equiaxed ferrite and granular carbides, while the Al-containing steels exhibited a microstructure of ferrite and granular bainite. The microstructural change observed upon adding Al to 5Cr steel is primarily due to the influence of Al on the phase transformation. Al suppresses the formation of carbides and promotes the formation of bainite, which is more stable and finer compared to the coarse carbides in the base steel. Additionally, Al refines the grain structure, contributing to the formation of granular bainite instead of large carbides, thus enhancing the steel's overall properties.

2.2 Corrosion tests

Corrosion tests were conducted in a 5 L high-pressure autoclave (Fig. 1). Before the experiment, the salt solution (Table 2) was purged with N_2 for 10 hours to remove dissolved O_2. Specimens measuring 20 × 10 × 3 mm^3 were sequentially polished with 500–2000 grit sandpaper, then cleaned with deionized water and acetone, air-dried, and their dimensions and weights recorded. The solution was introduced into the bottom of the autoclave at room temperature and atmospheric pressure, and the vessel was sealed. CO_2 gas was continuously bubbled into the autoclave for 2 hours to displace residual O_2. The system was then heated to 50 °C, and the pressure was maintained at 8.0 MPa using a booster pump. The corrosion experiment began when the temperature and pressure stabilized and was conducted under static conditions for 168 hours.

2.3 Weight loss tests and localized corrosion measurements

After the experiment, corrosion products were removed according to ASTM G1-03 (A solution was prepared by dissolving 3.5 g of hexamethylene tetramine in 500 mL of hydrochloric acid, and deionized water was added to bring the total volume to 1000 mL. The cleaning process was carried out for 10 minutes at a temperature range of 20 to 25 °C.), and the specimens were weighed to determine weight loss. The average corrosion rate was calculated using the eqn (1):

$$V_{corr} = \frac{87600\Delta m}{S\rho t} \quad (1)$$

where V_{corr} is the corrosion rate, mm per year; Δm is the weight loss, g; S is the exposed area of the samples, cm^2; ρ is the density of the steel, g cm^{-3}; and t is the exposure time, h. The final average corrosion rate was an average of three parallel specimens.

Localized corrosion rates were determined in accordance with ASTM G46-94. The average depth of the ten deepest corrosion pits was used to quantify localized corrosion performance (eqn (2)).

$$R_L = \frac{0.365h}{t} \quad (2)$$

where R_L is the localized corrosion rate, mm per year; h is the average depth of the ten deepest corrosion pits, μm; and t is the exposure time, d.

2.4 Characterization of the corrosion product scale

The morphology and elemental distribution of the corrosion products were analyzed using scanning electron microscopy (SEM) coupled with energy-dispersive X-ray spectroscopy (EDS). Additionally, the corrosion product compositions were further characterized through X-ray diffraction (XRD) and Raman spectroscopy using a 532 nm laser.

3 Results and discussion

3.1 Corrosion morphology

After a 168 hours corrosion test in water-saturated sc-CO_2, the surface morphology of Fe-5Cr-(0–3)Al alloy steels exhibited significant changes with increasing Al content (Fig. 2). The surface of the 5Cr steel was covered by a dense corrosion product layer, which displayed multiple bulging structures, indicative of severe localized pitting corrosion. This result is consistent with the findings reported by Hua *et al.*[15] and L. Wei *et al.*[13] As the Al content increased, the sample color lightened, and the localized bulging significantly diminished (Fig. 2a–d).

SEM analysis revealed that the corrosion product films on the sample surfaces exhibited circular structures. In the case of 5Cr steel, the corrosion products were relatively large and densely packed. As the Al content increased, the corrosion product particles became smaller and more dispersed. Under water-saturated sc-CO_2 conditions, it remains unclear whether this corrosion phenomenon is driven by electrochemical reactions or gas-phase chemical reactions. During electrochemical processes, the formation of an electrolyte on the steel surface is a prerequisite. Once the solubility limit is exceeded, water molecules aggregate on the steel surface, forming a distinct liquid phase. Subsequently, sc-CO_2 dissolves into the liquid

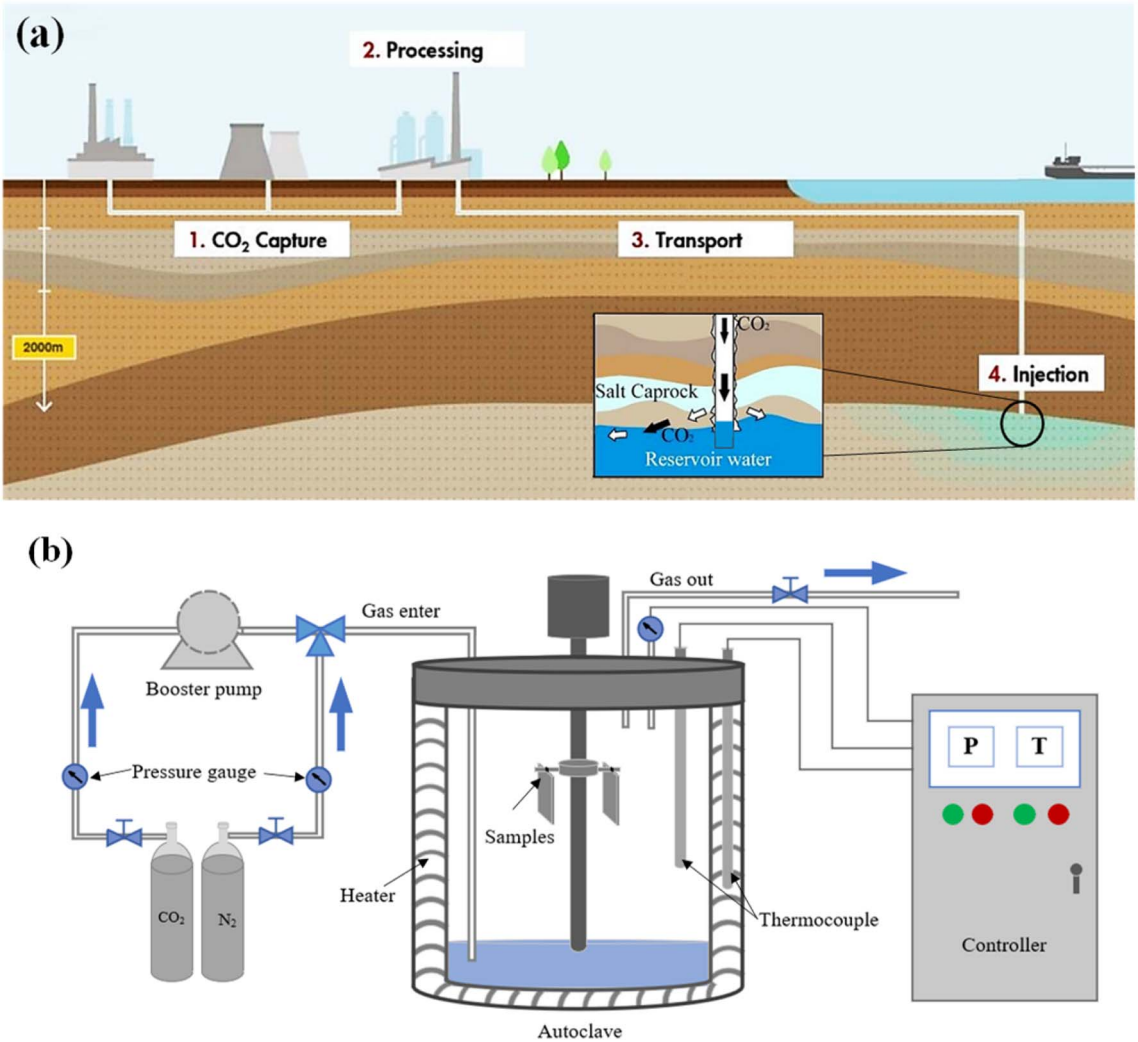

Fig. 1 Diagram showing an example of the CCUS process: modified from https://Shell.com (a)[26] and experimental setup for the high-pressure corrosion tests (b).

phase, generating carbonic acid (eqn (3) and (4)), which may result in severe corrosion of the pipelines.

$$CO_2 + H_2O \rightarrow H_2CO_3 \quad (3)$$

$$H_2CO_3 \rightarrow CO_3^{2-} + 2H^+ \quad (4)$$

It is worth noting that the cathodic reaction pathway is closely related to the solution's pH. When pH > 4, the direct reduction of carbonic acid (reaction (5)) dominates, whereas reaction (6) becomes more significant when pH < 4.[27] In water-saturated sc-CO_2 environments, the pH of the liquid droplets is below 4, making reaction (6) the primary cathodic reaction pathway.[28] The resulting iron ions then react with carbonate or bicarbonate ions to form $FeCO_3$ (eqn (7) and (8)).

$$H_2CO_3 + e^- \rightarrow HCO_3^- + H \quad (pH > 4) \quad (5)$$

$$H^+ + e^- \rightarrow H \quad (pH < 4) \quad (6)$$

$$Fe \rightarrow Fe^{2+} + 2e^- \quad (7)$$

$$Fe^{2+} + CO_3^{2-} \rightarrow FeCO_3 \quad (8)$$

Apart from electrochemical reactions, corrosion in sc-CO_2 environments may also proceed through gas-phase chemical processes, as mentioned earlier. In gas-phase chemical corrosion, the formation of liquid water is no longer essential; instead, H_2O dissolved in sc-CO_2 can directly react with steel to form iron oxides. Theoretical calculations suggest that among various iron oxides, only FeO can further react with CO_2 to

Table 2 Chemical composition of formation water extracted from gas condensate field

Composition	NaCl	$CaCl_2$	KCl	$MgCl_2 \cdot 6H_2O$	$NaHCO_3$	Na_2SO_4
Content (mmol L^{-1})	432.8	24.8	8.6	9.5	6.2	1.4

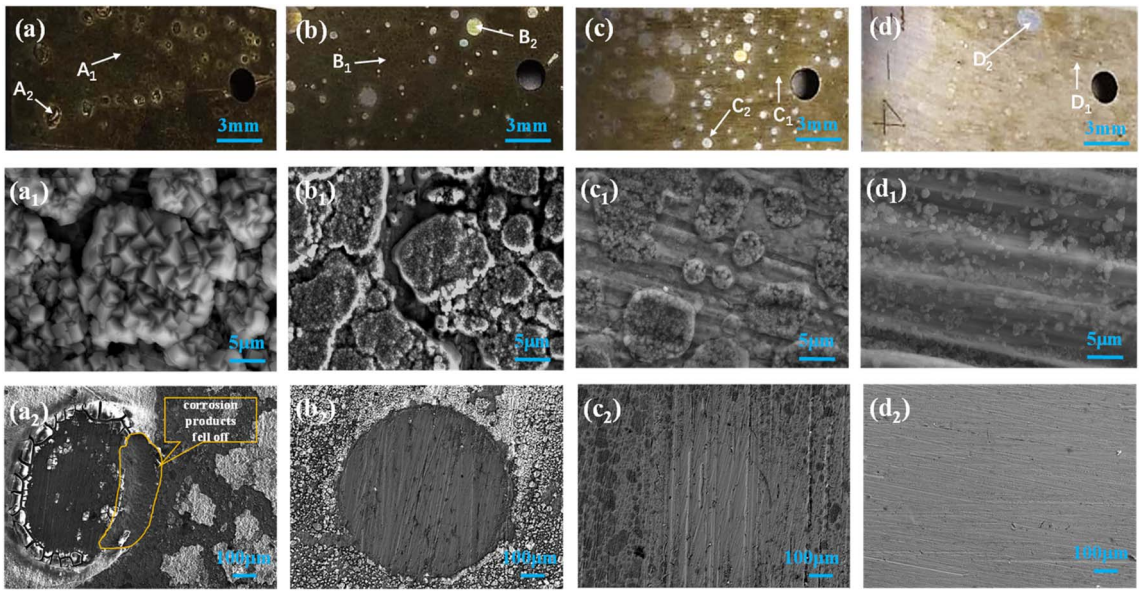

Fig. 2 (a) 5Cr, (b) 5Cr1Al, (c) 5Cr2Al, and (d) 5Cr3Al show the macroscopic morphologies of the alloys after corrosion. Corresponding SEM images of regions (A_1–D_1) are shown in (a_1–d_1), and SEM images of regions (A_2–D_2) are presented in (a_2–d_2).

produce $FeCO_3$. The reaction is represented as follows: (eqn (9) and (10)).[29,30]

$$Fe + H_2O(g) \rightarrow FeO + H_2 \quad (9)$$

$$FeO + CO_2 \rightarrow FeCO_3 \quad (10)$$

Fig. $2a_2$–d_2 reveals the localized corrosion phenomena induced by free water precipitation in a sc-CO_2 environment. SEM results demonstrate that the corrosion products are densely distributed at the outer edge of the droplet, whereas the interior contains relatively sparse corrosion products. Surface profile analyses after the removal of corrosion products (Fig. 3a–d) further validate the macroscopic and microscopic observations. Localized corrosion regions in 5Cr and 5Cr1Al steels exhibited prominent ring-shaped pits, indicating more concentrated corrosion products and severe degradation in these areas. Among them, the depth of the corrosion pits in 5Cr steel reached approximately 30 μm. In contrast, no similar corrosion grooves were detected in 5Cr2Al and 5Cr3Al steels. Additionally, polishing marks on the steel surface remained clearly visible (Fig. $2a_1$–d_1). This observation is consistent with the microstructural analysis shown in Fig. 2, confirming that Al alloying completely suppressed localized corrosion in 5Cr-based steel.

3.2 Corrosion rate

Fig. 3e illustrates the average corrosion rates of Fe-5Cr-(0–3)Al alloy steels. As the Al content increased, the average corrosion rate decreased significantly. When the Al content reached 2 wt%, the decline in the corrosion rate plateaued, indicating that a moderate amount of Al effectively enhanced corrosion resistance. The comparison of localized corrosion rates (Fig. 3f) corroborates these findings. The average pit depths for 5Cr and 5Cr1Al steels were 23.07 μm and 11.20 μm, respectively, corresponding to localized corrosion rates of 1.23 mm per year and 0.58 mm per year. No corrosion pits were detected in 5Cr2Al and 5Cr3Al steels, resulting in a localized corrosion rate of 0. This demonstrates that the addition of Al not only reduced the average corrosion rate but also effectively suppressed localized corrosion. The localized corrosion rate exceeded the average corrosion rate by more than six times, highlighting that low-Cr alloy steel primarily undergoes localized corrosion in water-saturated sc-CO_2 environments. Compared to standard 5Cr steel, the addition of 2 wt% Al resulted in a 68% decrease in the average corrosion rate, while completely inhibiting localized corrosion. Parallel tests on 9Cr steel revealed comparable corrosion resistance to 5Cr3Al steel in sc-CO_2 environments, with an average corrosion rate of 0.03 mm per year and no occurrence of localized corrosion. However, 5Cr3Al steel offers significantly lower cost, higher cost-effectiveness, and superior machinability, making it a promising candidate for long-distance CO_2 pipeline applications.

3.3 Characteristics of corrosion products

The incorporation of Al significantly enhanced the corrosion resistance of Fe-5Cr-(0–3)Al alloy steel, a mechanism elucidated through the composition and distribution of the corrosion products. Raman spectroscopy identified $FeCO_3$ as the predominant corrosion product, with characteristic peaks at 182, 282, and 1082 cm^{-1}. Additionally, small amounts of $Cr(OH)_3$, characterized by a peak at 731 cm^{-1},[13] were detected in 5Cr and 5Cr1Al steels (Fig. 4a). The highest peak intensities were observed in 5Cr steel, indicating the thickest corrosion product layer and the most severe corrosion. With increasing Al content, the intensities of these characteristic peaks diminished, signifying a notable reduction in the formation of

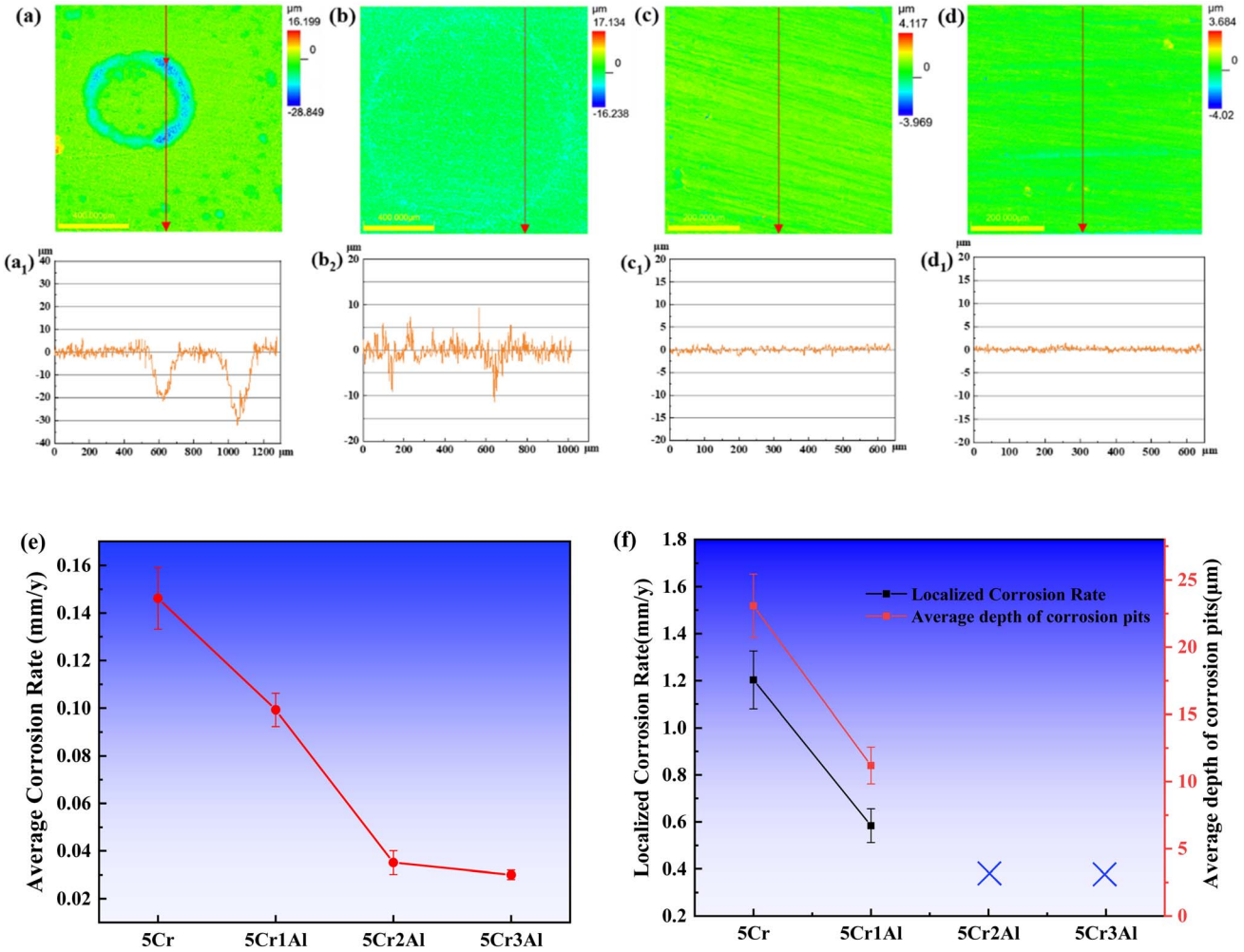

Fig. 3 Surface morphologies and linear profiles of Fe-5Cr-(0–3)Al alloys after removal of corrosion products: (a) and (a_1) 5Cr; (b) and (b_1) 5Cr1Al; (c) and (c_1) 5Cr2Al; (d) and (d_1) 5Cr3Al. (e) Presents the average corrosion rates and (f) shows the localized corrosion rates and average pit depths.

corrosion products. Among the alloys studied, the surface of 5Cr3Al steel exhibited the least amount of corrosion products, aligning with the SEM results presented in Fig. 2.

Fig. 4b illustrates the XRD analysis of the corrosion product films. For 5Cr steel, strong diffraction peaks were primarily attributed to $FeCO_3$ crystals. Raman spectroscopy further confirmed the presence of minor amounts of amorphous $Cr(OH)_3$. The low intensity of Fe substrate peaks in this alloy indicated a thick corrosion product layer. In contrast, 5Cr3Al steel showed an absence of diffraction peaks corresponding to

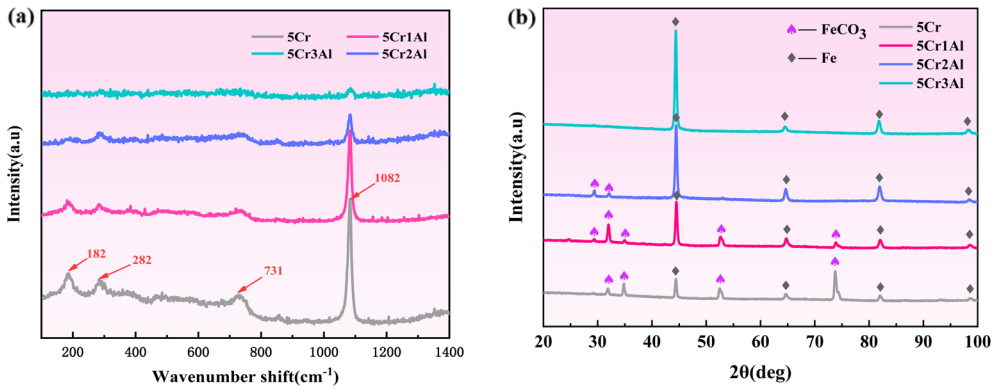

Fig. 4 Raman spectrum (a) and XRD spectrum (b) of the surface corrosion product film of Fe-5Cr-(0–3)Al alloy steels after 168 hours of immersion in water-saturated sc-CO_2 phase.

$FeCO_3$ or $Cr(OH)_3$, with only diffraction peaks related to elemental Fe being detected. This observation suggests an extremely thin and uniformly distributed corrosion product film on the surface of 5Cr3Al steel, corroborating the Raman spectroscopy findings. These results underscore the critical role of Al microalloying in mitigating the aggregation of corrosion products and promoting the uniformity of the protective film, thereby providing superior corrosion resistance.

3.4 Corrosion mechanism

The high extraction capability of sc-CO_2 facilitates the dissolution of significant amounts of water vapor into the sc-CO_2 phase. When the water content exceeds its solubility limit, free water precipitates and adheres to the material surface, where it reacts with CO_2 to form carbonic acid, intensifying localized corrosion. As shown in Fig. 5a–a_4, the corrosion products in the outer ring of localized corrosion pits are enriched in Cr and O elements, whereas the Fe content is relatively low. Atomic ratio analysis indicates that the outer-ring products are primarily composed of $Cr(OH)_3$ with minor amounts of $FeCO_3$, consistent with findings in the literature.[31] The formation of $Cr(OH)_3$ lowers the local pH, accelerating Fe dissolution. The corrosion products in the outer ring are significantly enriched, exhibiting a cracked morphology after dehydration. These products are loosely structured, relatively thick, and prone to detachment. In contrast, the inner-ring products are thinner, denser, and less likely to detach.

The formation of localized corrosion in 5Cr steel is primarily driven by two key factors. The interface between the water

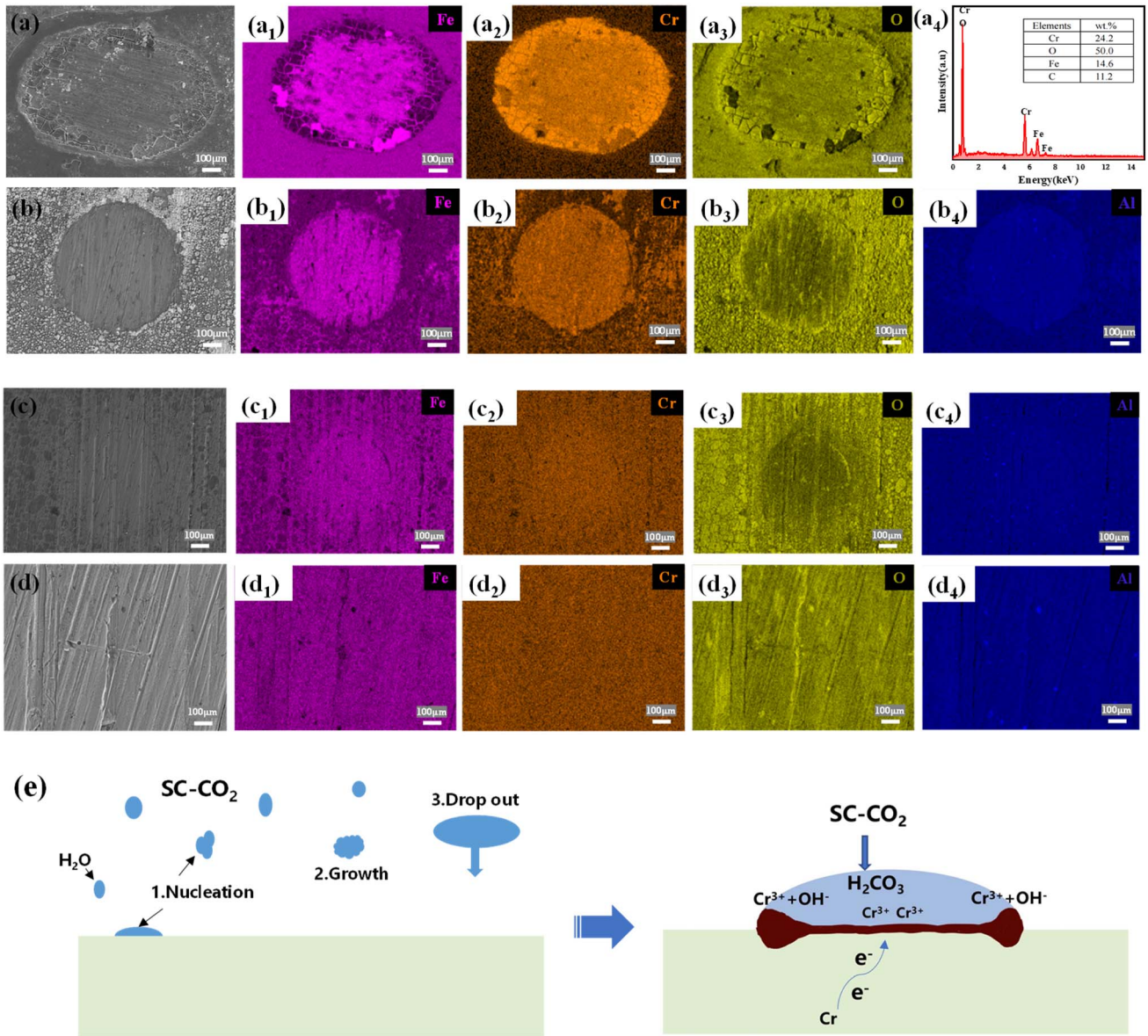

Fig. 5 SEM-EDS mappings of localized corrosion areas in Fe-5Cr-(0–3)Al alloy steels: (a–a_4) 5Cr; (b–b_4) 5Cr1Al; (c–c_4) 5Cr2Al; (d–d_4) 5Cr3Al, and localized corrosion mechanism diagram (e).

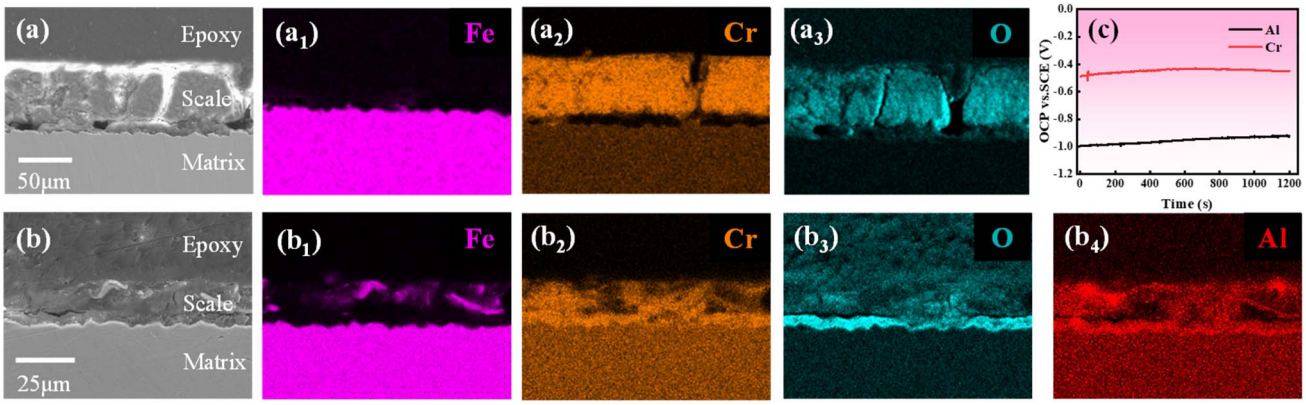

Fig. 6 SEM-EDS cross-sectional analysis of corrosion product layers in free water under sc-CO_2 environment. (a–a_3) 5Cr; (b–b_4) 5Cr2Al. (c) Open-circuit potential monitoring results of Cr and Al metals.

droplet and the metal surface is where corrosion is most likely to initiate, as the outer edges of the droplet experience direct exposure to sc-CO_2. This exposure causes CO_2 to dissolve and form carbonic acid, significantly lowering the pH (eqn (7)–(10)) and accelerating corrosion.[32] In contrast, the pH within the droplet's inner region remains higher, leading to milder corrosion conditions. Concurrently, a chemical composition gradient develops during corrosion, where the concentration of Cr^{3+} in the droplet's inner ring is much higher than at the outer edge. Driven by this gradient, Cr^{3+} diffuses outward and reacts with OH^- to form precipitates (eqn (11) and (12)), further contributing to the localized corrosion. So the localized corrosion features observed in 5Cr steel can be attributed to two key factors: the acidic environment at the edge of the droplet and the gradient in chemical composition across the surface.

$$Cr \rightarrow Cr^{3+} + 3e^- \quad (11)$$

$$Cr^{3+} + 3OH^- \rightarrow Cr(OH)_3 \quad (12)$$

With increasing Al content, the distribution of substrate elements becomes more uniform, indicating a gradual suppression of localized corrosion (Fig. 5b–d). This behavior can be attributed to two primary mechanisms related to the presence of Al. First, during the early stages of corrosion, aluminum undergoes hydrolysis, forming a dense $Al(OH)_3$ film that significantly mitigates corrosion caused by CO_2 and free water.[24,33,34] Second, the presence of Al inhibits the formation of $Cr(OH)_3$, which prevents a substantial decrease in the local pH, thereby reducing the occurrence of pitting corrosion.

Due to the excellent corrosion resistance exhibited by Fe-5Cr-(1–3)Al alloy steels in a water-saturated sc-CO_2 environment, the corrosion product layer is very thin, making it impossible to conduct a detailed *in situ* analysis of the corrosion mechanisms. Therefore, to further validate the corrosion resistance mechanism of Al, we simulated the corrosion behavior under the same conditions in a supercritical CO_2-saturated brine environment. As shown in the results of Fig. 6a and b, the corrosion product layer on 5Cr steel shows a uniform distribution of Cr and O elements, while the corrosion product layer on 5Cr2Al steel shows an additional enrichment of Al elements, with a gradient distribution from the inner to the outer layers. Combined with the open-circuit potential monitoring results of Cr and Al metals (Fig. 6c), it can be inferred that during the corrosion process, Al has higher chemical activity than Cr, leading to the preferential formation of $Al(OH)_3$ (eqn (13)), which forms a protective layer that effectively hinders further corrosion and suppresses the occurrence of localized corrosion. This result is consistent with the speculation made in the previous section.

$$2Al + 6H_2O \rightarrow 2Al(OH)_3 + 3H_2 \quad (13)$$

4 Conclusions

By incorporating 1–3 wt% Al into 5Cr steel, a series of novel low-Cr alloys were developed, demonstrating the corrosion resistance potential of Al in such alloys. When the Al content reaches 2 wt%, the average corrosion rate is reduced by 68% compared to 5Cr steel, and localized corrosion is fully suppressed. Al forms a dense, uniform aluminum hydroxide protective film, which prevents CO_2 and free water-induced corrosion, inhibits the formation of $Cr(OH)_3$, and maintains a stable local environment, significantly improving the alloy's resistance to localized corrosion. Notably, 5Cr3Al steel outperforms 9Cr steel in both cost-effectiveness and performance, highlighting its potential as an optimized material for pipeline applications in CCUS technologies.

Data availability

The research data supporting this publication are available in a public repository. Access to the data requires a subscription. Further details about the data, including repository location and access procedures, can be provided upon request.

Author contributions

Fubing Liu: writing original draft preparation, methodology-software, investigation, formal analysis, supervision, writing

review and editing, data curation. Hangqi Li: validation, investigation, formal analysis, visualization, formal analysis, resources. Yunan Zhang: validation, investigation, formal analysis, visualization. Rongdie Zhu: investigation, methodology-software, formal analysis, supervision. Jinyang Zhu: conceptualization, writing review and editing, project administration, funding acquisition.

Conflicts of interest

The authors declare that they have no known competing financial interests or personal relationships that could have appeared to influence the work reported in this paper.

Acknowledgements

This work was supported by the National Natural Science Foundation of China under grant No. 52101071.

References

1 R. L. Siegelman, E. J. Kim and J. R. Long, Porous materials for carbon dioxide separations, *Nat. Mater.*, 2021, **20**(8), 1060–1072.
2 H. B. Lee, H. H. Sheu, J. S. Jian, *et al.*, Sc-CO_2 electroless nickel plating enhanced anti-corrosion properties of micro-arc oxidized AZ31 magnesium alloy, *Mater. Today Commun.*, 2022, **33**, 104475.
3 H. Sun, H. Wang, Y. Zeng, *et al.*, Corrosion challenges in supercritical CO_2 transportation, storage, and utilization—a review, *Renewable Sustainable Energy Rev.*, 2023, **179**, 113292.
4 S. Sim, I. S. Cole, Y. S. Choi, *et al.*, A review of the protection strategies against internal corrosion for the safe transport of supercritical CO_2 *via* steel pipelines for CCS purposes, *Int. J. Greenhouse Gas Control*, 2014, **29**, 185–199.
5 C. Li, Y. Xiang, C. Song, *et al.*, Assessing the corrosion product scale formation characteristics of X80 steel in supercritical CO_2-H_2O binary systems with flue gas and NaCl impurities relevant to CCUS technology, *J. Supercrit. Fluids*, 2019, **146**, 107–119.
6 G. Cui, Z. Yang, J. Liu, *et al.*, A comprehensive review of metal corrosion in a supercritical CO_2 environment, *Int. J. Greenhouse Gas Control*, 2019, **90**, 102814.
7 B. Wang, M. Du, J. Zhang, *et al.*, Corrosion inhibition of mild steel by the hydrolysate of an imidazoline-based inhibitor in CO2-saturated solution, *RSC Adv.*, 2019, **9**(63), 36546–36557.
8 H. Li, D. Li, L. Zhang, *et al.*, Fundamental aspects of the corrosion of N80 steel in a formation water system under high CO2 partial pressure at 100 C, *RSC Adv.*, 2019, **9**(21), 11641–11648.
9 Y. Hua, S. Xu, Y. Wang, *et al.*, The formation of $FeCO_3$ and Fe_3O_4 on carbon steel and their protective capabilities against CO_2 corrosion at elevated temperature and pressure, *Corros. Sci.*, 2019, **157**, 392–405.
10 Y. Hua, R. Jonnalagadda, L. Zhang, *et al.*, Assessment of general and localized corrosion behavior of X65 and 13Cr steels in water-saturated supercritical CO_2 environments with SO_2/O_2, *Int. J. Greenhouse Gas Control*, 2017, **64**, 126–136.
11 M. Xu, Q. Zhang, Z. Wang, *et al.*, Cross impact of CO_2 phase and impurities on the corrosion behavior for stainless steel and carbon steel in water-containing dense CO_2 environments, *Int. J. Greenhouse Gas Control*, 2018, **71**, 194–211.
12 Y. Hua, R. Barker, T. Charpentier, *et al.*, Relating iron carbonate morphology to corrosion characteristics for water-saturated supercritical CO_2 systems, *J. Supercrit. Fluids*, 2015, **98**, 183–193.
13 L. Wei, K. Gao and Q. Li, Corrosion of low alloy steel containing 0.5% chromium in supercritical CO_2-saturated brine and water-saturated supercritical CO_2 environments, *Appl. Surf. Sci.*, 2018, **440**, 524–534.
14 S. Sim, I. S. Cole, Y. S. Choi, *et al.*, A review of the protection strategies against internal corrosion for the safe transport of supercritical CO_2 *via* steel pipelines for CCS purposes, *Int. J. Greenhouse Gas Control*, 2014, **29**, 185–199.
15 Y. Hua, R. Barker and A. Neville, Effect of temperature on the critical water content for general and localised corrosion of X65 carbon steel in the transport of supercritical CO_2, *Int. J. Greenhouse Gas Control*, 2014, **31**, 48–60.
16 S. Sim, F. Bocher, I. S. Cole, *et al.*, Investigating the effect of water content in supercritical CO_2 as relevant to the corrosion of carbon capture and storage pipelines, *Corrosion*, 2014, **70**(2), 185–195.
17 S. Hassani, T. N. Vu, N. R. Rosli, *et al.*, Wellbore integrity and corrosion of low alloy and stainless steels in high pressure CO_2 geologic storage environments: An experimental study, *Int. J. Greenhouse Gas Control*, 2014, **23**, 30–43.
18 Y. Y. Li, Z. Z. Wang, X. P. Guo, *et al.*, Galvanic corrosion between N80 carbon steel and 13Cr stainless steel under supercritical CO_2 conditions, *Corros. Sci.*, 2019, **147**, 260–272.
19 Y. Xiang, C. Song, C. Li, *et al.*, Characterization of 13Cr steel corrosion in simulated EOR-CCUS environment with flue gas impurities, *Process Saf. Environ. Prot.*, 2020, **140**, 124–136.
20 D. B. Yun, H. R. Bang, W. K. Kim, *et al.*, Effect of alloying (Cr, Mo, and V) on corrosion behaviors of API-grade steel in CO_2-saturated aqueous solutions with different pH, *J. Ind. Eng. Chem.*, 2024, **129**, 435–444.
21 Y. Hua, X. Yue, H. Liu, *et al.*, The evolution and characterisation of the corrosion scales formed on 3Cr steel in CO_2-containing conditions relevant to geothermal energy production, *Corros. Sci.*, 2021, **183**, 109342.
22 Z. Yuling, T. Qingchao, D. Xuyan, *et al.*, The CO_2 corrosion behaviour of 25Mn2 and 2Cr steels under certain downhole condition, *Corros. Eng., Sci. Technol.*, 2024, **59**(1), 3–12.
23 Y. Hua, S. Mohammed, R. Barker, *et al.*, Comparisons of corrosion behaviour for X65 and low Cr steels in high pressure CO_2-saturated brine, *J. Mater. Sci. Technol.*, 2020, **41**, 21–32.

24 Z. Gao, Y. Liu, C. Wang, *et al.*, The study on the influence of aluminum on the CO_2 corrosion resistance of 3% Cr steel, *Anti-Corros. Methods Mater.*, 2022, **69**(2), 177–182.
25 F. Liu, Q. Tang, Y. Zhang, *et al.*, Effect of Al content on mechanical properties and corrosion performance of novel Fe-Cr-Al alloy steels in a CO_2-O_2 coexistence environment, *J. Alloys Compd.*, 2025, **1010**, 177217.
26 *Sustainability-report*, 2016, **https://Shell.com**.
27 J. B. Sun, G. A. Zhang, W. Liu, *et al.*, The formation mechanism of corrosion scale and electrochemical characteristic of low alloy steel in carbon dioxide-saturated solution, *Corros. Sci.*, 2012, **57**, 131–138.
28 J. Zhu, L. Xu, M. Lu, *et al.*, Cathodic reaction mechanisms in CO_2 corrosion of low-Cr steels, *Int. J. Miner., Metall. Mater.*, 2019, **26**, 1405–1414.
29 Y. Zeng, X. Pang, C. Shi, *et al.*, *Influence of Impurities on Corrosion Performance of Pipeline Steels in Supercritical Carbon dioxide[C]//NACE CORROSION*, NACE, 2015, NACE-2015-5755.
30 K. Li and Y. Zeng, Advancing the mechanistic understanding of corrosion in supercritical CO_2 with H_2O and O_2 impurities, *Corros. Sci.*, 2023, **213**, 110981.
31 L. Wei and K. Gao, Understanding the general and localized corrosion mechanisms of Cr-containing steels in supercritical CO_2-saturated aqueous environments, *J. Alloys Compd.*, 2019, **792**, 328–340.
32 H. Hong, T. Ye, J. Zhang, *et al.*, Corrosion mitigation behavior of mild steel in supercritical CO_2 environments with varying the solution volume, *Corros. Sci.*, 2024, **229**, 111853.
33 R. Wang, S. Luo, M. Liu, *et al.*, Electrochemical corrosion performance of Cr and Al alloy steels using a J55 carbon steel as base alloy, *Corros. Sci.*, 2014, **85**, 270–279.
34 K. Xhanari, M. Finšgar, M. K. Hrnčič, *et al.*, Green corrosion inhibitors for aluminium and its alloys: a review, *RSC Adv.*, 2017, **7**(44), 27299–27330.